The Astrophysical Journal Letters, 1010:L21 (7pp), 2026 October 20 https://doi.org/10.3847/2041-8213/aea84b
© 2026. The Author(s). Published by the American Astronomical Society.
OPEN ACCESS

Nonlocal Evolution of Magnetic Helicity across the Magnetohydrodynamic–Kinetic Interface

Masatomi Iizawa[1], Yasuhito Narita[1,2], Tommaso Alberti[3], Stuart D. Bale[4,5], Axel Brandenburg[6,7,8,9], Abraham C.-L. Chian[10,11], Horia Comişel[12], Shuichi Matsukiyo[13,14,15,16], and Nobumitsu Yokoi[6,17,18,19]
[1] Institut für Theoretische Physik, Technische Universität Braunschweig, Mendelssohnstr. 3, D-38106 Braunschweig, Germany; masatomi.iizawa@tu-braunschweig.de
[2] Max Planck Institute for Solar System Research, Justus-von-Liebig-Weg 3, D-37077 Göttingen, Germany
[3] Istituto Nazionale di Geofisica e Vulcanologia, via di Vigna Murata 605, 00143 Rome, Italy
[4] Space Sciences Laboratory, University of California, Berkeley, CA 94720-7450, USA
[5] Physics Department, University of California, Berkeley, CA 94720-7300, USA
[6] Nordita, KTH Royal Institute of Technology and Stockholm University, 10691 Stockholm, Sweden
[7] The Oskar Klein Centre, Department of Astronomy, Stockholm University, 10691 Stockholm, Sweden
[8] School of Natural Sciences and Medicine, Ilia State University, 0194 Tbilisi, Georgia
[9] McWilliams Center for Cosmology and Department of Physics, Carnegie Mellon University, Pittsburgh, Pennsylvania 15213, USA
[10] School of Computer and Mathematical Sciences, Adelaide University, Adelaide, SA 5005, Australia
[11] National Institute for Space Research (INPE), P.O. Box 515, São José dos Campos, São Paulo 12227-010, Brazil
[12] Institute for Space Sciences, Atomiştilor 409, P.O. Box MG-23, Bucharest-Măgurele, RO-077125, Romania
[13] Faculty of Engineering Sciences, Kyushu University, Kasuga, Fukuoka 816-8580, Japan
[14] Quantum and Spacetime Research Institute (QuaSR), Kyushu University, Motooka, Nishi-ku, Fukuoka 819-0395, Japan
[15] International Research Center for Space and Planetary Environmental Science (i-SPES), Kyushu University, Motooka, Nishi-ku, Fukuoka 819-0395, Japan
[16] Institute of Laser Engineering, Osaka University, Suita, Osaka 565-0871, Japan
[17] Department of Earth and Planetary Science, University of Tokyo, 7-3-1 Hongo, Bunkyo, Tokyo 113-0033, Japan
[18] Institute of Fluid Science, Tohoku University, 2-1-1, Katahira, Aoba-ku, Sendai 980-8577, Japan
[19] Laboratoire de Mécanique des Fluides et d'Acoustique (LMFA), UMR5509, Université de Lyon, École Centrale de Lyon, CNRS, Université Claude Bernard Lyon 1, INSA Lyon, 36 Avenue Guy de Collonge, 69130 Écully, France
Received 2026 July 7; revised 2026 August 28; accepted 2026 September 15; published 2026 October 13

Abstract

Magnetic helicity is typically indistinguishable from noise in the solar wind inertial range. Using Parker Solar Probe measurements (0.1–0.8 au), we report a robust bihelical structure emerging at the magnetohydrodynamic (MHD)–kinetic interface. This structure, formed by a striking pair of positive and negative peaks, exhibits a systematic spectral migration toward lower frequencies with increasing heliocentric distance. Crucially, this evolution deviates from local kinetic scaling laws, such as the radial decline of the ion cyclotron frequency, reflecting a nonlocal evolution of magnetic topology. Our findings provide a new observational constraint on both nonlocal MHD transport processes and the nature of the helicity barrier in the kinetic regime.

Unified Astronomy Thesaurus concepts: Solar wind (1534); Interplanetary magnetic fields (824); Solar physics (1476)

1. Introduction

The solar wind provides a dynamic laboratory for studying the transition from magnetohydrodynamic (MHD) to kinetic plasma turbulence (R. Bruno & V. Carbone 2013). A fundamental quantity in this transition is magnetic helicity, which characterizes the topological complexity of magnetic fields. While MHD theory treats helicity as a rugged invariant (W. H. Matthaeus & M. L. Goldstein 1982; W. H. Matthaeus et al. 1982; M. Brown et al. 1999), its fate at the ion kinetic scales, where fluid descriptions fail and wave–particle interactions dominate, remains a frontier of plasma physics (T. A. Bowen et al. 2020). Traditionally, helical fluctuations at sub-ion scales have been interpreted as local wave modes, such as ion cyclotron waves (ICWs) or kinetic Alfvén waves (KAWs), governed by the local plasma environment (R. J. Leamon et al. 1998; J. J. Podesta 2013). However, recent theoretical developments, most notably the helicity barrier (R. Meyrand et al. 2021; J. Squire et al. 2022), suggest that the interplay between magnetic helicity and kinetic damping can fundamentally alter the energy cascade, potentially leading to the accumulation or redistribution of helical signatures across scales.

Magnetic helicity is often dismissed as stochastic noise within the MHD inertial range (W. H. Matthaeus et al. 1982; C. W. Smith 2003). Consequently, the recent identification of helical peaks near ion kinetic scales was a major surprise (R. J. Leamon et al. 1998; J. J. Podesta 2013; D. Telloni et al. 2015; T. Alberti et al. 2022b). These signatures, however, have remained snapshots confined to specific local plasma conditions. Tracking their radial evolution was impossible for earlier missions like Helios (W. H. Matthaeus & M. L. Goldstein 1982) and Voyager (R. Bruno & M. Dobrowolny 1986), which lacked the sampling rates to probe the sub-ion regime above 10^{-2} Hz. It remains a fundamental missing link whether these structures are merely transient local fluctuations or part of a broader, nonadiabatic transformation. In this Letter, we exploit the high-resolution magnetic field measurements obtained by the Parker Solar Probe (PSP) during its deep penetration into the inner heliosphere. By analyzing the magnetic helicity spectra at frequencies above 1 Hz, we identified robust bihelical structures that migrate systematically across heliocentric distances. Our study primarily focuses on the quantified discrepancy between

Original content from this work may be used under the terms of the Creative Commons Attribution 4.0 licence. Any further distribution of this work must maintain attribution to the author(s) and the title of the work, journal citation and DOI.

the observed drift and the local kinetic scaling laws, suggesting a fundamentally nonlocal evolution of magnetic topology at the MHD–kinetic interface.

2. Methodology and Its Validity

We estimated the magnetic helicity density spectrum (W. H. Matthaeus & M. L. Goldstein 1982; W. H. Matthaeus et al. 1982; Y. Narita et al. 2009) using data from the FIELDS fluxgate magnetometer (S. D. Bale et al. 2016) on PSP (N. J. Fox et al. 2016). We focused on data collected from 2021 September 29, 00:00:00 UTC, to 2021 November 22, 00:00:00 UTC, a period characterized by short sampling intervals and a wide radial swing from 0.100 to 0.782 au in 0.002 au increments. For each increment, 1 hr of data was collected, with sampling intervals of 3441 μs (0.100–0.160 au), 6827 μs (0.162–0.260 au), and 109 227 μs (0.262–0.782 au), which affect the acquirable frequency bands. Cubic spline interpolation addressed $\sim$1 μs fluctuations in sampling intervals. The data with inconsistent sample counts per hour were treated as missing, especially beyond 0.434 au. The reduced normalized magnetic helicity density spectra σ_m (W. H. Matthaeus & M. L. Goldstein 1982; W. H. Matthaeus et al. 1982; Y. Narita 2023), defined as

$$\sigma_m = \frac{2\mathrm{Im}[\langle b_T^* b_N \rangle]}{\langle |b_T|^2 \rangle + \langle |b_N|^2 \rangle}, \quad (1)$$

were calculated using magnetic fields b_T and b_N in the RTN coordinate system in the frequency domain, which are transformed using fast Fourier transform (FFT), i.e., $b_T(f) = \sum_{t=0}^{L-1} \exp(-2\pi jft/L) B_T(t)$ where L is the number of samples in the time domain, and $B_T(t)$ and $b_N(f)$ represent the magnetic field in the time and frequency domain, respectively. The normal component $b_N(f)$ is defined analogously. $\langle |b_T|^2 \rangle$ and $\langle |b_N|^2 \rangle$ represent the power spectral density. This definition yields a positive sign for helicity when it is right-handed with respect to the radial outward direction, consistent with the definition of the cross-spectral density, for example, *complex coherence* in signal processing (D. Ramírez et al. 2022), though opposite to J. J. Podesta & S. P. Gary (2011). Spectral density estimation employed Welch's method with a Hanning window (P. Welch 1967). It is important to emphasize that σ_m is a reduced quantity derived from single-spacecraft time series under Taylor's frozen-in hypothesis (TH) (G. I. Taylor 1938). This metric σ_m specifically measures the sense of magnetic field rotation (polarization) around the radial sampling direction (D. Telloni et al. 2015). Consequently, due to the inherent limitations of single-point measurements, this approach does not capture the full three-dimensional helicity, as it excludes fluctuations and wavevectors associated with the radial component (W. H. Matthaeus & M. L. Goldstein 1982; Y. Narita et al. 2009).

To assess the validity of TH used for the wavenumber transformation, we evaluate the effects of both random sweeping and wave propagation in the plasma frame. Figure 1 displays the radial evolution of the dimensionless parameter $\epsilon = \delta u_0/(\sqrt{2}\, V_\perp)$ and the Doppler shift factor assuming Alfvén waves $1 + V_A/V_\perp$, where $V_\perp$ is the spacecraft velocity component perpendicular to the local magnetic field in the plasma frame (J. C. Perez et al. 2021). The parameter ϵ quantifies the ratio of the velocity

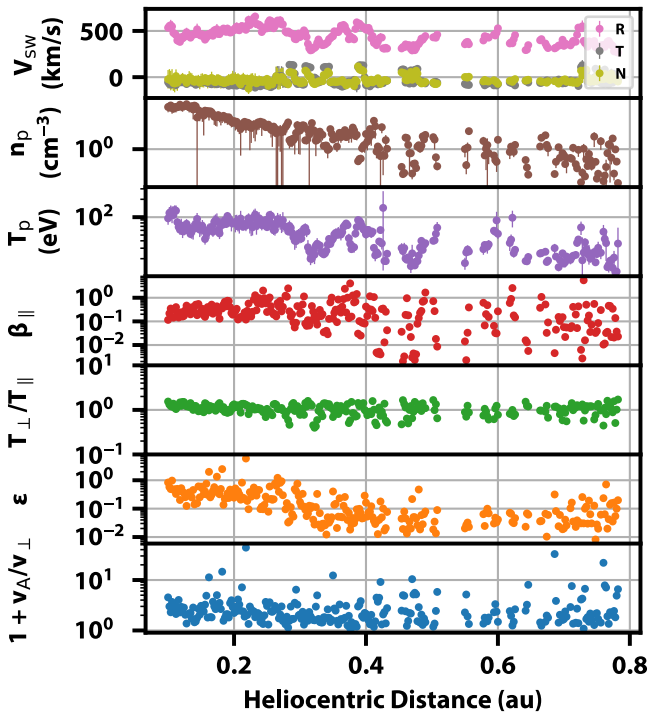


Figure 1. Radial evolution of plasma parameters and Taylor hypothesis diagnostics. Panels display (from top to bottom) solar wind flow speed V_{sw}, proton density n_p, proton temperature T_p, parallel proton beta $\beta_\parallel$, and temperature anisotropy $T_\perp/T_\parallel$. The bottom panels show the sweeping parameter ϵ and the Doppler shift factor $1 + V_A/V_\perp$ (see text for definitions), used to assess the validity of the Taylor frozen-in hypothesis. All parameters are averaged over 1 hr intervals. Missing data points are omitted from the plots.

fluctuations at the energy-containing scale δu_0 to the sampling speed. As shown in Figure 1, ϵ decreases from $\approx$0.3 near the perihelion ($\approx$0.1 au) to $\approx$0.03 at larger distances ($\approx$0.7 au). This radial trend is in excellent agreement with theoretical predictions for the inner heliosphere (S. Bourouaine & J. C. Perez 2019). We used the standard deviation of velocity fluctuations for δu_0 without applying the moving average filter used by J. C. Perez et al. (2021). Since our method includes fluctuations from all measured scales, the ϵ values in Figure 1 represent a conservative upper bound. The actual sweeping effect is likely smaller, reinforcing the validity of the TH as ϵ decreases to $\ll$1 with distance. In the near-Sun region, the relatively high ϵ values ($\gtrsim$0.5) and the low Alfvén Mach number regime suggest that the strict frozen-in condition may be violated, potentially subjecting the frequency-to-wavenumber mapping to spectral broadening. However, theoretical models and numerical simulations demonstrate that even under strong sweeping (large ϵ), the spectral index of the frequency spectrum remains identical to that of the underlying wavenumber spectrum (M. Wilczek & Y. Narita 2012; S. Bourouaine & J. C. Perez 2018). Thus, our estimates of magnetic helicity spectral slopes remain robust against the deviations from TH. We note that the plasma parameters were obtained from PSP's SPAN-I (R. Livi et al. 2022). While partial field-of-view obstruction may cause underestimation of proton moments during radial flow (R. Livi et al. 2022), such systematic offsets act primarily as linear scaling factors and cannot reproduce the observed order-of-magnitude radial migration addressed in this study. Regarding spatial scales, the factor $1 + V_A/V_\perp$ fluctuates between 1 and 4, with a mean of approximately 2.5. This indicates that due to the nonnegligible

phase speed of Alfvénic fluctuations in low-Mach-number flows (K. G. Klein et al. 2014), the derived wavenumbers may be overestimated (and physical scales underestimated) by a factor of ∼2.5. Nevertheless, as we investigate spectral features spanning multiple orders of magnitude, this factor-of-a-few shift is negligible relative to the broad spectral evolution. Furthermore, this implies that changes in the sampling angle θ_{BV} cannot drive order-of-magnitude systematic trends, as its effect via $V_\perp$ is secondary.

The radial evolution of magnetic helicity signatures can originate from several nonlocal processes, such as nonlinear mode coupling across distinct scales, large-scale advection, or the emergence of a helicity barrier. In the classical framework of MHD turbulent transport, these processes are typically quantified by the time evolution of the magnetic helicity density spectrum $H_M(k, t) = \mathrm{Re} \oint_{|\boldsymbol{k}|=\mathrm{k}} \hat{\boldsymbol{A}}_{\boldsymbol{k}} \cdot \hat{\boldsymbol{B}}^*_{\boldsymbol{k}} \mathrm{d}\Omega(\boldsymbol{k})$ where $d\Omega(\boldsymbol{k}) = k^2 \sin\theta d\theta d\phi$. That is,

$$\frac{\partial}{\partial t} H_M(k, t) = 2S_M(k, t) - 2\eta k^2 H_M(k, t), \tag{2}$$

where $S_M(k, t)$ is the transfer function defined as $\mathrm{Re} \oint_{|\boldsymbol{k}|=\mathrm{k}} \hat{\mathcal{E}}_{\boldsymbol{k}} \cdot \hat{\boldsymbol{B}}^*_{\boldsymbol{k}} \mathrm{d}\Omega(\boldsymbol{k})$, using the electromotive force $\hat{\mathcal{E}}_{\boldsymbol{k}} = \widehat{\boldsymbol{u} \times \boldsymbol{B}}$, and magnetic diffusivity η (A. Brandenburg 2001; W.-C. Müller & S. K. Malapaka 2013). The spectral flux of magnetic helicity is defined as

$$G_M(k, t) = \int_k^\infty 2S_M(k', t) dk'. \tag{3}$$

Because S_M is the third-order moment of the velocity field $\boldsymbol{u}$ and the magnetic field $\boldsymbol{B}$, its direct computation requires high-sampling-rate data on the velocity field $\boldsymbol{u}$. However, in tenuous plasma environments, particle instruments must scan energy and direction, which fundamentally limits the sampling rate; consequently, obtaining velocity spectra at or above the order of 1 Hz remains unfeasible (A. W. Case et al. 2020; R. Livi et al. 2022; L. B. Wilson et al. 2022). Alternatives to this direct approach also face significant hurdles. Using the fluctuating electric field $\boldsymbol{E}$ as a proxy for the electromotive force $\boldsymbol{u} \times \boldsymbol{B}$ is unreliable below 100 Hz due to antenna characteristics and the plasma environment around the spacecraft (T. Imachi et al. 2007; J. J. Podesta 2013; D. P. Hartley et al. 2017; S. Karbashewski et al. 2023). Furthermore, approximating $\boldsymbol{E}$ using the generalized Ohm's law within the framework of electron MHD (EMHD) requires the current density $\boldsymbol{j} = \nabla \times \boldsymbol{B}$, which necessitates multipoint spatial derivatives, which are inaccessible to single-spacecraft measurements (K.-H. Glassmeier et al. 2001; Y. Narita et al. 2009). Given these constraints, a direct calculation of S_M in the region of interest is currently impossible. Furthermore, the applicability of this MHD-based description to the MHD–kinetic interface remains theoretically unverified. Regardless of the underlying framework, the systematic spectral migration of helicity signatures reflects the integrated effect of all local and nonlocal transport processes.

3. Results

The magnetic field power spectral density (PSD) shown in Figure 2 consistently exhibits an inertial subrange characterized by a Kolmogorov $-5/3$ energy decay, aligning with

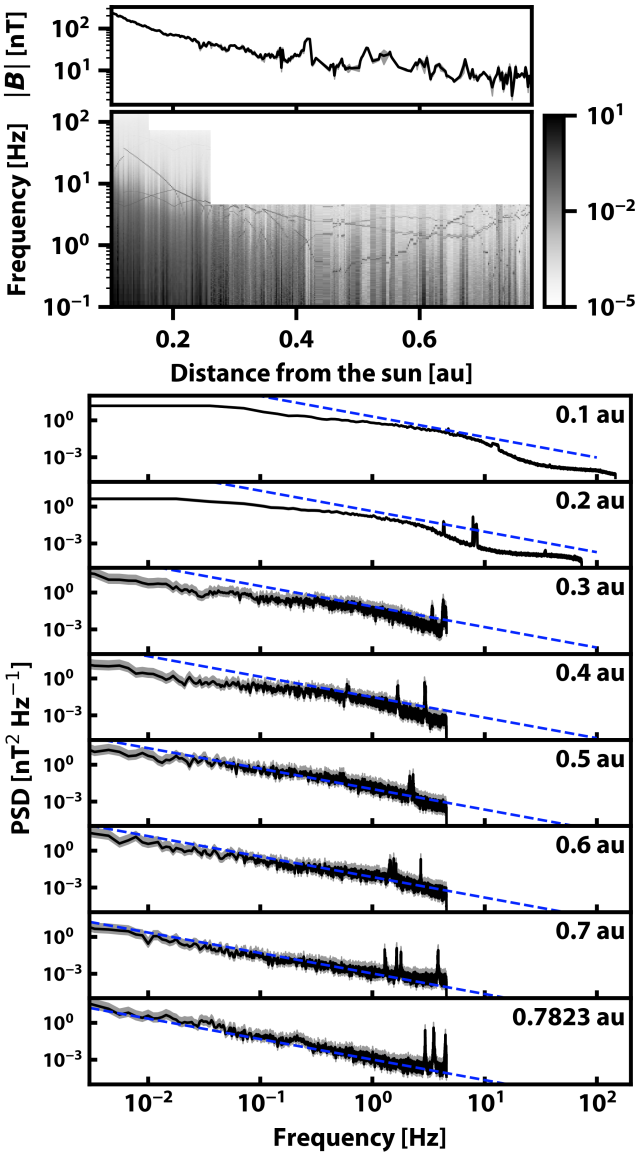


Figure 2. Radial evolution of magnetic field intensity and power spectral density. (Top) Magnetic field magnitude $|\boldsymbol{B}|$ as a function of heliocentric distance. The gray shaded region represents the standard deviation calculated over the 1 hr intervals. (Middle) PSD of magnetic field fluctuations shown as a color map in the frequency–distance plane. The spectra are computed via Welch's method with a segment length of 2^{13} points. (Bottom) Representative 1D spectra at seven heliocentric distances, extracted from the middle panel. Blue dashed lines denote a $-5/3$ spectral index for reference. Deviations from this scaling are visible as the spacecraft approaches the Sun.

previous observations (J. J. Podesta 2013; C. H. K. Chen et al. 2020; T. Alberti et al. 2022b). Notably, at 0.1 au, our high-sampling-rate measurements extended the observable frequency band by approximately 2 orders of magnitude compared to conventional datasets. However, the dissipation range remains uncaptured, suggesting that the Kolmogorov scale exceeds 2×10^2 Hz. While previous studies have reported that the spectral index approaches $-3/2$ as heliocentric distance decreases, with a significant transition occurring around 0.4–0.6 au (C. H. K. Chen et al. 2020), our statistical analysis generally supports this trend. It is worth noting, however, that the radial evolution of turbulence can be sensitive to the sampling method. While statistical surveys across diverse solar wind streams typically show this spectral

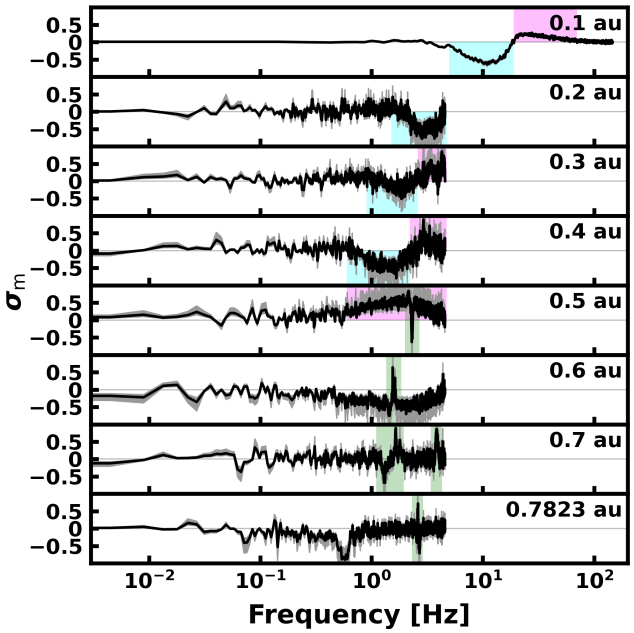


Figure 3. Normalized magnetic helicity density spectra σ_m in the spacecraft frame. The spectra are computed via Welch's method (segment length 2^{13}), with gray shaded regions indicating 95% confidence intervals. Red and blue areas represent positive and negative helicity, respectively, while green areas denote suspected instrumental artifacts. Note that individual intervals may capture periods of transiently low wave amplitude due to the inherent intermittency of solar wind turbulence (R. Bruno & V. Carbone 2013; V. K. Jagarlamudi et al. 2021; C. Froment et al. 2023). The comprehensive evolution of these modes across the inner heliosphere is further detailed in Figure 4.

evolution, D. Perrone et al. (2022) observed a more stable spectral slope when tracking a single plasma parcel from the same coronal source. Although our study adopts a statistical approach consistent with C. H. K. Chen et al. (2020), resolving the discrepancy between these Eulerian and Lagrangian perspectives remains beyond the scope of this Letter. Proposed mechanisms for this radial transition include the breakdown of self-similarity (a monofractal to multifractal transition) (T. Alberti et al. 2020) and the evolving coupling between velocity and magnetic field fluctuations (T. Alberti et al. 2022a).

More significantly, the normalized magnetic helicity density spectra, as exemplified in Figure 3, reveal a prominent negative peak at 10 Hz and a positive peak at 20 Hz at 0.1 au. The statistical significance of these peaks is confirmed by 95% confidence intervals that exclude zero. As the heliocentric distance increases, these peaks continuously shift to lower frequencies. This trend is clearly depicted in the top panel of Figure 4. This shift, observed across 0.1–0.4 au, provides a characteristic observational signature of the systematic growth of helical structures toward larger spatial scales. While some peaks appear to vanish at intermediate distances (e.g., 0.2 au), this is an observational artifact caused by lower sampling rates in survey mode rather than a physical disappearance of the mode; these peaks reemerge in the observable band beyond 0.3 au, exhibiting a continuous shift toward lower frequencies. Beyond approximately 0.5 au, this clear helicity structure becomes less discernible. Minor fluctuations in spectral shift reflect the influence of transient events, as measurements across different distances are not concurrent. While some sharp, narrow peaks are considered

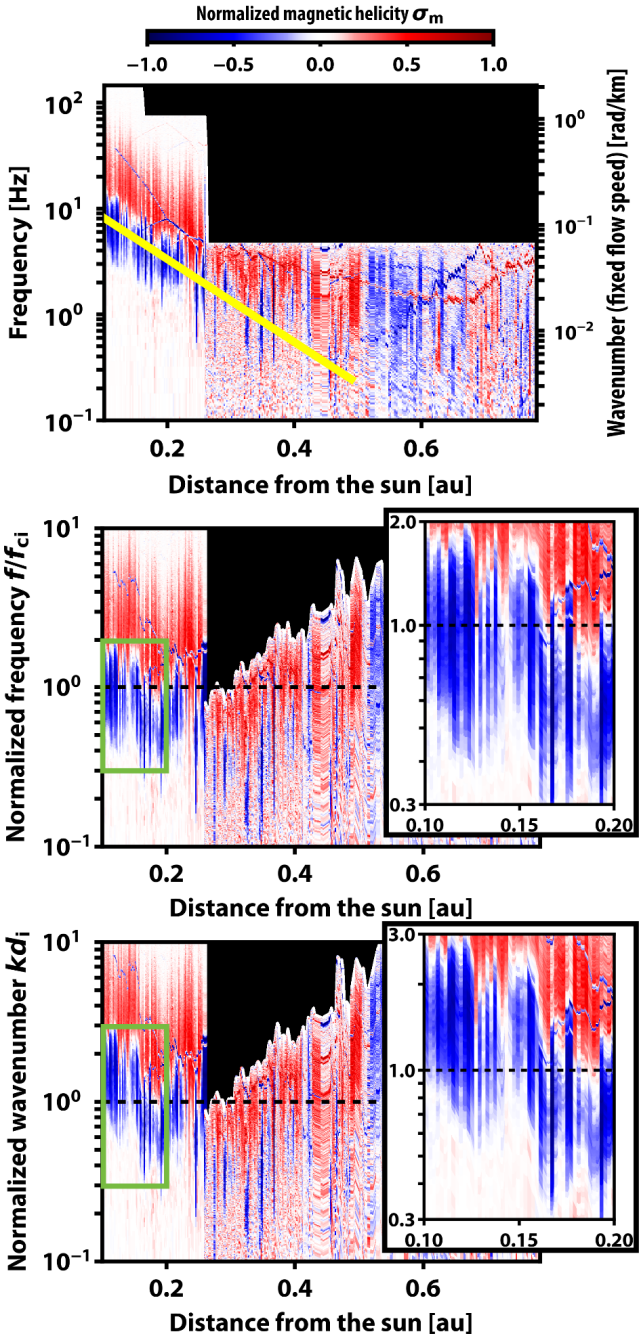


Figure 4. Radial evolution of magnetic helicity and characteristic scale scaling. (Top) Color map of the reduced normalized magnetic helicity density σ_m in the frequency–distance plane. Black regions indicate data gaps due to low sampling rates. The yellow line is $f = f_0 \exp(-\lambda r)$, where $f_0 = 20$ Hz and $\lambda = 9$ au^{-1} serve as a rough guide for the observed spectral migration. The right-hand axis provides an indicative wavenumber scale based on a constant solar wind speed $V_{sw} = 441.4$ km s^{-1} (the average of the moment data); this axis serves as an order-of-magnitude reference. (Middle) Spectra normalized by the local proton cyclotron frequency, f/f_{ci}. The inset shows an enlarged view of the green-outlined area. (Bottom) Spectra normalized by the ion inertial length, kd_i. Despite the scatter induced by variable local conditions, the helicity peaks in the normalized plots do not collapse onto a fixed scale (e.g., $f/f_{ci} \sim$ const. or $kd_i \sim$ const.). Instead, they exhibit a systematic migration toward larger scales relative to the local ion scales as distance increases.

instrumental artifacts, and others may capture solar events spanning several weeks, these factors do not alter our fundamental conclusions. This study does not aim to prove the ubiquity of these phenomena in the inner heliosphere, but

rather to demonstrate their feasibility and empirical occurrence.

In Figure 4, the middle and bottom panels display the spectra normalized by the local proton cyclotron frequency f_{ci} and the wavenumber scaled by the ion inertial length $k\,d_i$, respectively. These normalizations serve to test whether the characteristic scales of magnetic helicity are governed primarily by local plasma instabilities. If the helical structures were generated and sustained purely by local kinetic processes, such as ion cyclotron or kinetic Alfvén instabilities observed in previous studies (J. He et al. 2011; T. A. Bowen et al. 2020; S. Y. Huang et al. 2020; D. Duan et al. 2021), the spectral peaks would be expected to collapse onto a constant characteristic scale (e.g., $f/f_{ci} \sim$ const. or $k\,d_i \sim$ const.) regardless of the heliocentric distance. However, as clearly visualized in the enlarged insets of Figure 4, the helical structures do not remain horizontally aligned with these local kinetic scales. Instead, the peaks systematically cross the constant-scale reference lines ($f/f_{ci} = 1$ and $kd_i = 1$) and exhibit a systematic migration toward larger scales.

While a unified turbulent diffusion scale (e.g., $k(\rho_p + d_i) \sim 1$; D. Duan et al. 2020a, 2020b) or the boundary of the turbulence ion diffusion range (T-IDR) (J. He et al. 2020) provides a comprehensive physical boundary incorporating both dissipation and dispersion at the MHD–kinetic transition, we retain normalizations by individual parameters. The unified scale is derived from the parallel cyclotron resonance condition, and applying it to highly anisotropic solar wind turbulence introduces geometrical ambiguities. Furthermore, since the normalizations by both f_{ci} and d_i independently exhibit the same exponential spectral migration, the combined local scales would inevitably show an identical systematic slippage. This slippage of the energy-containing scale relative to the characteristic kinetic scales provides a compelling observational signature that the helical structures are not merely static local features but are dynamically evolving.

4. Discussion and Conclusion

To properly interpret the observed dynamics of magnetic helicity, it is crucial to distinguish between the local injection (the seed) of helical fluctuations and their subsequent nonlocal evolution (transport). To understand the origin of the distinct positive and negative helicity peaks observed between 0.1 and 0.4 au, the most compelling seed mechanism is the excitation by proton temperature anisotropy (J. J. Podesta & S. P. Gary 2011). Specifically, pressure anisotropy ($T_{p\perp}/T_{p\parallel} > 1$) triggers left-hand polarized ICWs, while the firehose instability ($T_{p\perp}/T_{p\parallel} < 1$) excites right-hand polarized whistler waves. While the dispersion relation of L-mode waves exhibits ω-axis symmetry in the plasma frame, the Doppler shift in the spacecraft frame reduces the angular frequency ω for wavevectors $k < 0$ relative to $k > 0$, naturally producing the observed split in magnetic helicity signs. This interpretation is further supported by the fact that R-mode whistler waves typically emerge at smaller scales than L-mode waves. Conversely, alternative mechanisms such as parametric decay (L. Del Zanna et al. 2001; R. Bruno & V. Carbone 2013; A. Tenerani & M. Velli 2013; T. A. Bowen et al. 2018), though capable of increasing magnetic compressibility (C. H. K. Chen et al. 2020), would likely result in random mixing rather than the clearly separated helicity components observed here; furthermore, simulations indicate that Alfvén waves subject to parametric breakdown diminish significantly within a few solar radii (A. Tenerani & M. Velli 2013). Similarly, while mean-field dynamo theory predicts bihelical magnetic helicity (E. G. Blackman & A. Brandenburg 2003), it assumes hemispheric sign reversals at scales far exceeding those in our study (2–25 μHz) (A. Brandenburg et al. 2011), and the required latitudinal dependence remains unverifiable with current PSP data, awaiting future multispacecraft observations. Furthermore, recent observations by H. Xie et al. (2026) provide another compelling candidate for the local seeding of such bihelical signatures. They demonstrated that at the MHD–kinetic interface, quasi-perpendicular KAWs transfer energy to particles, which subsequently inject part of that energy into quasi-parallel ICWs.

Once injected, the dynamic nonlocal evolution of magnetic helicity is further corroborated by the specific functional form of the observed frequency shift. While adiabatic solar wind expansion can increase turbulence scales (E. Marsch & C. Y. Tu 1993; C. Y. Tu & E. Marsch 1993; R. Grappin & M. Velli 1996; M. L. Goldstein & D. A. Roberts 1999), simple expansion models based on the frozen-in hypothesis ($f \sim U_{sw}/d_i$) and Parker's density profile ($n \propto r^{-2}$) predict a power-law shift of $f \propto 1/r$. This fundamentally differs from our observed exponential decay, $f \propto \exp(-\lambda r)$, ruling out passive geometric expansion as the primary driver and pointing instead to nonlinear fluid interactions. Specifically, the accumulation of magnetic helicity at scales exceeding local ion scales aligns with the *helicity barrier* mechanism proposed for imbalanced KAW turbulence (R. Meyrand et al. 2021; J. Squire et al. 2022). This theory suggests that the transition from MHD to kinetic scales inhibits the forward energy cascade for high cross-helicity flows, forcing an inverse transfer and a pile-up of magnetic helicity at scales larger than the ion gyroradius. Consequently, the observed slippage of the helicity peak relative to ion scales (Figure 4, bottom) provides a compelling observational signature of this barrier preventing efficient dissipation of helical fluctuations. Although third-order scaling laws, such as Yaglom's law (Y. Wang & O. Chkhetiani 2023), offer rigorous tools for determining cascade directions (L. Sorriso-Valvo et al. 2007, 2023; G. Consolini et al. 2020; H. Wu et al. 2022, 2023), their application is precluded by the aforementioned sampling limitations. Relying on second-order spectral evolution, we find that the observed exponential migration poses a new challenge for theoretical modeling, as it deviates from the power-law evolution predicted by idealized EMHD simulations (H. Kim & J. Cho 2015). This discrepancy likely stems from the complex interplay between proton-scale dynamics and global expansion in the solar wind. Future studies should investigate how the contributions of individual terms in the MHD equations vary under these realistic conditions, potentially exploring the role of residual helicity, i.e., the difference between kinetic and current helicity, as suggested by residual energy analysis (N. Yokoi & F. Hamba 2007).

Finally, we address the observed disappearance of the magnetic helicity structure beyond 0.5 au. The proximity of PSP's orbit to the ecliptic plane (within $\pm 3.^{\circ}4$), combined with significant fluctuations in the magnetic field strength near 0.4–0.5 au, suggests that the spacecraft frequently crosses the heliospheric current sheet (HCS) (J. M. Wilcox & N. F. Ness 1965). Such interactions likely disrupt the transport

of helical fluctuations, potentially causing the coherent helicity signatures to vanish. To determine whether this disappearance represents a genuine spatial evolution or merely an orbital artifact caused by the HCS, future studies should extend this analysis using complementary data at larger heliocentric distances and higher latitudes obtained by the Solar Orbiter. In addition, this disappearance coincides with a reported transition in the radial dependence of energy spectra between 0.4 and 0.6 au (T. Alberti et al. 2020, 2022a), marking the shift from predominantly MHD turbulence near the Sun to a more hydrodynamic-like regime at larger distances. Critically, while traditional theories often neglect the nonlinear advection term when evaluating the influence of background magnetic fields (T. Alberti et al. 2022a), our results suggest that this term is indispensable. Moreover, the applicability of this MHD framework to the MHD–kinetic interface remains an open question. Our results demonstrate that the integrated effect of all underlying fundamental processes follows neither passive expansion nor local kinetic dissipation. Instead, the observed exponential migration serves as a quantitative constraint for future models to either incorporate kinetic-scale effects or extend current turbulence paradigms.

Acknowledgments

M.I. appreciates the insightful discussion with Prof. Uwe Motschmann (TU Braunschweig, Germany). We thank the anonymous referee for helpful comments and suggestions. The FIELDS experiment on the Parker Solar Probe spacecraft was designed and developed under NASA contract NNN06AA01C. We acknowledge the NASA Parker Solar Probe Mission and the SWEAP team led by J. Kasper for use of data. This work was funded by the Deutsche Forschungsgemeinschaft (DFG, German Research Foundation)—535057280 and also by the Japan Society for the Promotion of Science (JSPS) grants-in-Aid for Scientific Research JP23K25895 and JP26K00767. We acknowledge support by the Open Access Publication Funds of the Technische Universität Braunschweig.

Software and Data Availability

The codes used for the analysis and the plotted data are available in Zenodo at doi:10.5281/zenodo.22779133.

Facility: PSP.

Software: SunPy (SunPy Community et al. 2020; S. J. Mumford et al. 2025), Astropy (Astropy Collaboration et al. 2013, 2018, 2022), SpiceyPy (A. Annex et al. 2020), Polars (R. Vink et al. 2025), SciPy (P. Virtanen et al. 2020), NumPy (C. R. Harris et al. 2020), Matplotlib (J. D. Hunter 2007).

ORCID iDs

Masatomi Iizawa https://orcid.org/0000-0002-3735-0616
Yasuhito Narita https://orcid.org/0000-0002-5332-8881
Tommaso Alberti https://orcid.org/0000-0001-6096-0220
Stuart D. Bale https://orcid.org/0000-0002-1989-3596
Axel Brandenburg https://orcid.org/0000-0002-7304-021X
Abraham C.-L. Chian https://orcid.org/0000-0002-8932-0793
Horia Comişel https://orcid.org/0000-0002-5028-8482
Shuichi Matsukiyo https://orcid.org/0000-0002-4784-0301
Nobumitsu Yokoi https://orcid.org/0000-0002-5242-7634

References

Alberti, T., Benella, S., Consolini, G., Stumpo, M., & Benzi, R. 2022a, ApJL, 940, L13
Alberti, T., Laurenza, M., Consolini, G., et al. 2020, ApJ, 902, 84
Alberti, T., Narita, Y., Hadid, L. Z., et al. 2022b, A&A, 664, L8
Annex, A., Pearson, B., Seignovert, B., et al. 2020, JOSS, 5, 2050
Astropy Collaboration, Price-Whelan, A. M., Lim, P. L., et al. 2022, ApJ, 935, 167
Astropy Collaboration, Price-Whelan, A. M., Sipőcz, B. M., et al. 2018, AJ, 156, 123
Astropy Collaboration, Robitaille, T. P., Tollerud, E. J., et al. 2013, A&A, 558, A33
Bale, S. D., Goetz, K., Harvey, P. R., et al. 2016, SSRv, 204, 49
Blackman, E. G., & Brandenburg, A. 2003, ApJ, 584, L99
Bourouaine, S., & Perez, J. C. 2018, ApJL, 858, L20
Bourouaine, S., & Perez, J. C. 2019, ApJL, 879, L16
Bowen, T. A., Badman, S., Hellinger, P., & Bale, S. D. 2018, ApJL, 854, L33
Bowen, T. A., Mallet, A., Bale, S. D., et al. 2020, PhRvL, 125, 025102
Brandenburg, A. 2001, ApJ, 550, 824
Brandenburg, A., Subramanian, K., Balogh, A., & Goldstein, M. L. 2011, ApJ, 734, 9
Brown, M., Canfield, R., Field, G., et al. 1999, in Magnetic Helicity in Space and Laboratory Plasmas, ed. M. R. Brown, R. C. Canfield, & A. A. Pevtsov (American Geophysical Union), 301
Bruno, R., & Carbone, V. 2013, LRSP, 10, 2
Bruno, R., & Dobrowolny, M. 1986, AnGeo, 4, 17
Case, A. W., Kasper, J. C., Stevens, M. L., et al. 2020, ApJS, 246, 43
Chen, C. H. K., Bale, S. D., Bonnell, J. W., et al. 2020, ApJS, 246, 53
Consolini, G., Alberti, T., & Carbone, V. 2020, Entrp, 22, 1419
Del Zanna, L., Velli, M., & Londrillo, P. 2001, A&A, 367, 705
Duan, D., Bowen, T. A., Chen, C. H. K., et al. 2020b, ApJS, 246, 55
Duan, D., He, J., Bowen, T. A., et al. 2021, ApJL, 915, L8
Duan, D., He, J., Wu, H., & Verscharen, D. 2020a, ApJ, 896, 47
Fox, N. J., Velli, M. C., Bale, S. D., et al. 2016, SSRv, 204, 7
Froment, C., Agapitov, O. V., Krasnoselskikh, V., et al. 2023, A&A, 672, A135
Glassmeier, K.-H., Motschmann, U., Dunlop, M., et al. 2001, AnGeo, 19, 1439
Goldstein, M. L., & Roberts, D. A. 1999, PhPl, 6, 4154
Grappin, R., & Velli, M. 1996, JGRA, 101, 425
Harris, C. R., Millman, K. J., van der Walt, S. J., et al. 2020, Natur, 585, 357
Hartley, D. P., Kletzing, C. A., Kurth, W. S., et al. 2017, JGRA, 122, 4420
He, J., Marsch, E., Tu, C., Yao, S., & Tian, H. 2011, ApJ, 731, 85
He, J., Zhu, X., Verscharen, D., et al. 2020, ApJ, 898, 43
Huang, S. Y., Zhang, J., Sahraoui, F., et al. 2020, ApJL, 897, L3
Hunter, J. D. 2007, CSE, 9, 90
Imachi, T., Yagitani, S., Higashi, R., & Nagano, I. 2007, JElCo, 90, 45
Jagarlamudi, V. K., Dudok de Wit, T., Froment, C., et al. 2021, A&A, 650, A9
Karbashewski, S., Agapitov, O. V., Kim, H. Y., et al. 2023, ApJ, 947, 73
Kim, H., & Cho, J. 2015, ApJ, 801, 75
Klein, K. G., Howes, G. G., & TenBarge, J. M. 2014, ApJL, 790, L20
Leamon, R. J., Smith, C. W., Ness, N. F., Matthaeus, W. H., & Wong, H. K. 1998, JGRA, 103, 4775
Livi, R., Larson, D. E., Kasper, J. C., et al. 2022, ApJ, 938, 138
Marsch, E., & Tu, C. Y. 1993, JGRA, 98, 21045
Matthaeus, W. H., & Goldstein, M. L. 1982, JGRA, 87, 6011
Matthaeus, W. H., Goldstein, M. L., & Smith, C. 1982, PhRvL, 48, 1256
Meyrand, R., Squire, J., Schekochihin, A., & Dorland, W. 2021, JPlPh, 87, 535870301
Müller, W.-C., & Malapaka, S. K. 2013, GApFD, 107, 93
Mumford, S. J., Freij, N., Stansby, D., et al. 2025, sunpy: A Core Package for Solar Physics, v7.0.1, Zenodo, doi:10.5281/zenodo.16638197
Narita, Y. 2023, GMS, 283, 105
Narita, Y., Kleindienst, G., & Glassmeier, K.-H. 2009, AnGeo, 27, 3967
Perez, J. C., Bourouaine, S., Chen, C. H. K., & Raouafi, N. E. 2021, A&A, 650, A22
Perrone, D., Perri, S., Bruno, R., et al. 2022, A&A, 668, A189
Podesta, J. J. 2013, SoPh, 286, 529
Podesta, J. J., & Gary, S. P. 2011, ApJ, 734, 15
Ramírez, D., Santamaría, I., & Scharf, L. 2022, Coherence: In Signal Processing and Machine Learning (Springer)
Smith, C. W. 2003, AdSpR, 32, 1971
Sorriso-Valvo, L., Marino, R., Carbone, V., et al. 2007, PhRvL, 99, 115001
Sorriso-Valvo, L., Marino, R., Foldes, R., et al. 2023, A&A, 672, A13

Squire, J., Meyrand, R., Kunz, M. W., et al. 2022, NatAs, 6, 715
SunPy Community, Barnes, W. T., Bobra, M. G., et al. 2020, ApJ, 890, 68
Taylor, G. I. 1938, RSPSA, 164, 476
Telloni, D., Bruno, R., & Trenchi, L. 2015, ApJ, 805, 46
Tenerani, A., & Velli, M. 2013, JGRA, 118, 7507
Tu, C. Y., & Marsch, E. 1993, JGRA, 98, 1257
Vink, R., de Gooijer, S., Beedie, A., et al. 2025, pola-rs/polars: Python Polars v1.27.1, Zenodo, doi:10.5281/ZENODO.15194971
Virtanen, P., Gommers, R., Oliphant, T. E., et al. 2020, NaMet, 17, 261
Wang, Y., & Chkhetiani, O. 2023, PhD, 454, 133835
Welch, P. 1967, ITAuE, 15, 70
Wilcox, J. M., & Ness, N. F. 1965, JGR, 70, 5793
Wilczek, M., & Narita, Y. 2012, PhRvE, 86, 066308
Wilson, L. B., Goodrich, K. A., Turner, D. L., et al. 2022, FrASS, 9, 1063841
Wu, H., Tu, C., He, J., Wang, X., & Yang, L. 2022, ApJ, 927, 113
Wu, H., Tu, C., He, J., Wang, X., & Yang, L. 2023, PhPl, 30, 020501
Xie, H., He, J., Peng, J., & Wu, Z. 2026, ApJL, 1006, L53
Yokoi, N., & Hamba, F. 2007, PhPl, 14, 112904